

Micro Bubble Blanket Coated Nano-Ridge Surfaces for Robust and Efficient Thermal Management

Xiongjiang Yu,* Guohan Wu, Wenli Ye, Bo Zhang, and Jinliang Xu*

To achieve robust and high-efficient thermal management at micro scale, this study focuses on interplay of a micro bubble blanket and lifting large bubbles on locally heated surfaces with nano-ridge structures. The micro bubble blanket covers the surface dynamically after heat fluxes exceed a criterion where heat transfer coefficients exhibit constant values, highlighting the robust and predictable two-phase heat transfer. By quantitative investigations of diameters as well as lifting speed of large bubbles, it ensures that convective boiling heat transfer mechanism dominates without forced convection, accounting for constant heat transfer coefficient at high-heat-flux regions. Force analyses are adopted to investigate the individual micro bubbles that form the bubble blanket, which is pinned downside to nano-ridge surfaces by free energy while pulled upside by merging effect of buoyancy-driven large bubbles. The presence of the bubble blanket facilitates the removal of large bubbles by modifying the surface tension distribution, sustaining safe boiling heat transfer across a broad range of heat fluxes. This approach achieves a convective boiling mechanism without the need for power equipment, opening a new paradigm in microscale heat removal that is both robust and energy-efficient.

1. Introduction

Concurrently with the strides in chip performance, heat generation has also escalated significantly. Inefficient heat dissipation from chips can adversely affect both their performance and longevity.^[1] The traditional method of air-cooling is becoming progressively insufficient to address the cooling requirements of contemporary high-performance chips.^[2] In light of these challenges, immersion liquid cooling has emerged as a viable solution, notable for its high heat transfer efficiency and minimal energy consumption.^[3] This technology is bifurcated into single-phase and two-phase immersion cooling, based on the occurrence of phase changes within the coolant during the cooling process.^[4,5] Notably, two-phase immersion cooling stands

X. Yu, G. Wu, W. Ye, B. Zhang, J. Xu The Beijing Key Laboratory of Multiphase Flow and Heat Transfer for Low Grade Energy Utilization

North China Electric Power University

Beijing 102206, P. R. China

 $\hbox{E-mail: } yuxiong jiang@ncepu.edu.cn; xjl@ncepu.edu.cn\\$

The ORCID identification number(s) for the author(s) of this article can be found under https://doi.org/10.1002/smll.202411835

DOI: 10.1002/smll.202411835

out for its exceptional cooling efficiency, attributable to the nucleate boiling effect, positioning it as a potential successor to air cooling as the predominant chip cooling method in the future.

Achieving precise temperature control in chip cooling necessitates an accurate determination of the heat transfer coefficient at the fluid-heating surface interface.^[7] However, forecasting this coefficient in twophase immersion cooling presents a challenge due to the intricacies of nucleate boiling, a heat transfer process mediated by bubble nucleation, which entails a complex interplay of macroscopic and microscopic factors. Studies on the fundamentals of nucleate boiling have been underway since the 1930s, and three principal heat transfer mechanisms have been identified: (i) Transient Conduction,[8] where heat is rapidly transferred from the surface to the liquid as cool fluid replaces a departing bubble. (ii) Micro Convection,[9] which arises from fluid movement around the heating surface due to bubble nucleation,

growth, detachment, and ascent, thereby enhancing heat transfer. (iii) Microlayer Evaporation, [10] where heat transfer occurs through the evaporation of a thin liquid film at the base of an expanding bubble. High-resolution measurement techniques have facilitated a deeper understanding of these mechanisms' contributions under diverse conditions. Demiray et al. investigated FC-72 boiling using microheater arrays and high-speed imaging,[11] revealing that Microlayer Evaporation predominates at low subcooling, while Transient Conduction and Micro Convection gain importance at higher subcooling levels. Gerardi et al. employed a thin-film heater composed of indium tin oxide (ITO) and synchronized infrared and high-speed cameras to track bubble growth in water,[12] confirming the dominance of Transient Conduction in heat transfer. Yabuki et al. utilized a microelectromechanical system (MEMS) sensor to measure local temperature changes under isolated bubbles,[13] demonstrating that Microlayer Evaporation contributes to approximately half of the heat transfer during bubble growth. These studies underscore the intricacy of heat transfer prediction in nucleate boiling, as the mechanisms are intimately linked to bubble dynamics.^[14] Additionally, the critical heat flux (CHF), as a pivotal performance metric of two-phase immersion cooling technology, directly determines the safe operational limit of boiling systems. Exceeding CHF triggers an abrupt transition to film boiling, characterized

16136829, D. Dowlooladed from https://onlinelibtrary.wiely.com/doi/10.1002/smlt.202411835 by North China Electric Power University Beijing, Wiley Online Library on [231012025]. See the Terms and Conditions (https://onlinelibrary.wiely.com/terms-and-conditions) on Wiley Online Library for rules of use; OA articles are governed by the applicable Cerative Commons.

www.small-journal.com

by a drastic reduction in heat transfer coefficient and the risk of localized overheating. Recent advancements in surface micronano structure engineering have propelled CHF enhancement strategies to the forefront of research, with mechanistic studies centered on optimizing the balance between liquid replenishment and vapor escape. The copper microcavity and nanocone composite (CMN) developed by Ze et al. achieved a 64% CHF enhancement in water, driven by superhydrophilic properties that facilitate liquid supply.[15] However, this enhancement diminishes with prolonged microstructure growth time, revealing challenges in maintaining optimal structural parameter. Yu et al.'s investigation of artificial microcavity surfaces in FC-72 demonstrated that while high-density microcavity arrays significantly increase CHF, excessive cavity density conversely suppresses CHF due to bubble coalescence-induced vapor film formation.^[16] Ha and Graham engineered micropore architectures with vapor escape channels, achieving a CHF of 3500 kW/m² while restricting surface superheating to 49 °C, though the vapor layer growth mechanism within porous structures remains unresolved.[17] Despite the potential of surface modification techniques to enhance CHF, persistent challenges remain in addressing structural stability, multiscale heat transfer coupling, and adaptability to complex operational conditions during practical implementation, which substantially constraining the widespread adoption of two-phase immersion cooling technology.

In addressing the challenges outlined, this study introduces an innovative strategy based on active regulation of bubble dynamics. Utilizing microelectromechanical systems technology fabricated microheaters,[18] we perform pool boiling experiment using liquid carbon dioxide (15 °C, 5.7 MPa) as the coolant. The developed configuration synergizes nanoscale ridge surface architectures with the low surface tension of liquid carbon dioxide to induce vigorous micro bubble activity in high heat flux regions. To our surprise, this engineered system enables precise modulation of interactions between small and large bubbles, establishing robust and efficient heat transfer in high heat flux environments: On one hand, the absorption of micro bubbles by large bubbles establishes rapid vapor migration channels, effectively preventing heat transfer deterioration caused by vapor accumulation on heating surfaces. This non-structure-dependent vapor management strategy demonstrates excellent robustness and operational adaptability. On the other hand, the micro bubble blanket persistently reduces the gas-liquid interfacial contact line length for the lifting big bubbles, significantly diminishing surface tension constraints on bubble detachment. This mechanism profoundly influences bubble departure size and facilitates the establishment of stable flow field adjacent to the heating surface. Consequently, experimental results confirm that the heat transfer process under these conditions is predominantly convective, sustaining a stable heat transfer coefficient across a broad range of temperature, thus enabling predictable boiling heat transfer. The convection-dominated boiling generally occurs in flow boiling at high mass fluxes or vapor mass qualities in microchannels.[19-22] Here, we uniquely achieve it in pool boiling. Moreover, carbon dioxide boasts superior thermophysical properties, such as high thermal conductivity, density, latent heat, and specific heat capacity, coupled with low viscosity. It also presents additional advantages over other dielectric coolants, including inherent fire suppression capabilities and a low global warming potential (GWP).^[23] This study introduces a new perspective for the practical application of two-phase immersion cooling technology in industrial production.

2. Results and Discussion

Within the heat flux range of q = 0-9 MW m⁻², three distinct heat transfer regimes are delineated, as shown in Figure 1a. (i) Natural Convection (NC): In this regime, no bubbles nucleate on the heating surface, and as the heat flux (q) escalates, so does the wall superheat ($\Delta T_{\rm w}$). (ii) Nucleate Boiling (NB): At a critical heat flux of 0.912 MW m⁻², bubble formation initiates, signaling the onset of nucleate boiling (ONB). Here, the slope of the boiling curve steepens, enhancing heat transfer due to the cooling effect of bubble nucleation on the wall surface. (iii) Convective Boiling (CB): In this regime, as *q* further increases, the slope of the boiling curve starts to diminish. Figure 1b illustrates that the heat transfer coefficient (h) remains nearly constant rather than escalating with q. It is noteworthy that CHF is not encountered in this mode. Contrary to other pool boiling experiments where htypically decreases at elevated heat fluxes due to vapor film formation on the heating surface, the CB mode sustains enhanced heat transfer. This augmentation is ascribed to the synergistic interaction between micro and large bubbles in the CB region. Micro bubbles expedite the growth and detachment of large bubbles, [24] which in turn cools the microheater more efficiently. This phenomenon, where micro bubbles aid in the detachment of large bubbles at high heat fluxes, holds promise for mitigating CHFrelated heat transfer degradation.

2.1. Visual Images Analysis

2.1.1. Visual Images and Transient Wall Temperatures

In the low heat flux region of the Nucleate Boiling (NB) mode ($q=0.912-1.621~{\rm MW~m^{-2}}$), the transient wall temperature ($T_{\rm w}(t)$) and transient heat flux (q(t)) exhibit relatively minor fluctuations, as shown in **Figure 2a**. To elucidate the correlation between $T_{\rm w}(t)$ fluctuations and bubble nucleation more clearly, the fluctuations within the 770–790 ms interval were magnified (see Figure 2b). Visual observations (Figure 2c) indicate that bubbles nucleate, grow, and detach in a largely independent fashion. The variations in $T_{\rm w}(t)$ are influenced by the behavior of the bubbles. For instance, the reduction in $T_{\rm w}(t)$ observed during the time interval from 770.5 to 773.25 ms is attributed to the cooling effect as bubbles detach from the heating surface, permitting cool fluid to contact the wall surface. In this region, the predominant heat transfer mechanism is the nucleation of individual bubbles.

In the middle heat flux region of the Nucleate Boiling (NB) mode (q = 1.773-3.530 MW m⁻²), the fluctuations in $T_{\rm w}(t)$ and q(t) are similar to those observed in the low heat flux region, exhibiting minimal variation, as shown in **Figure 3a**. To delve into the nuances, the $T_{\rm w}(t)$ fluctuations within the 937–945 ms interval were magnified, leading to the visualization presented in Figure 3b. In this region, alongside the formation of large bubbles, distinct small bubbles are also observed at the base of the large bubbles (see Figure 3c). The fluctuations in $T_{\rm w}(t)$ are influenced not only by the nucleation, growth, and detachment of

16136829, 0, Downloaded from https://onlinelibrary.wiley.com/doi/10.1002/smll.202411835 by North China Electric Power University Beijing, Wiley Online Library on [23/10/2025]. See the Terms

nditions) on Wiley Online Library for rules of use; OA articles are governed by the applicable Creative Commons

www.small-journal.com

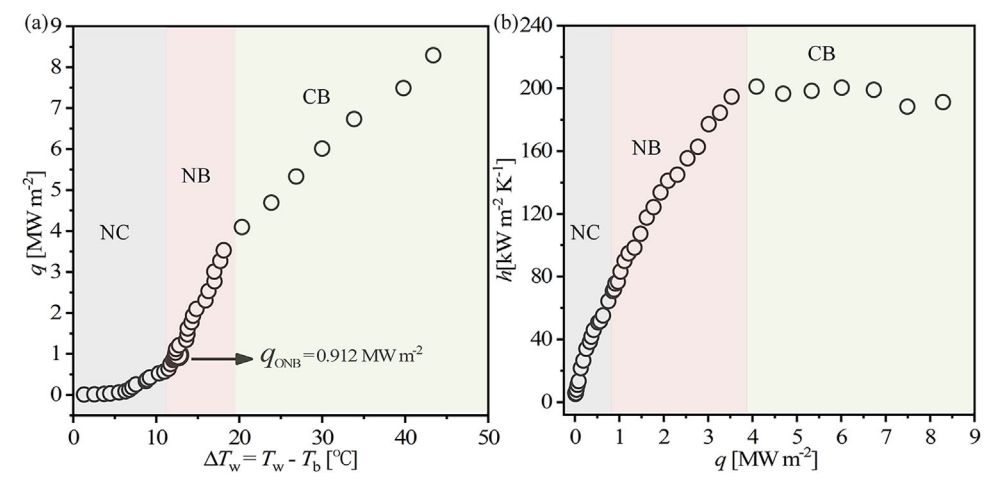


Figure 1. Heat transfer characteristics of the microheater with P = 5.7 MPa and $T_b = 15$ °C. a) Boiling curve of carbon dioxide (CO₂). b) heat transfer coefficients (h) dependent on heat flux (q).

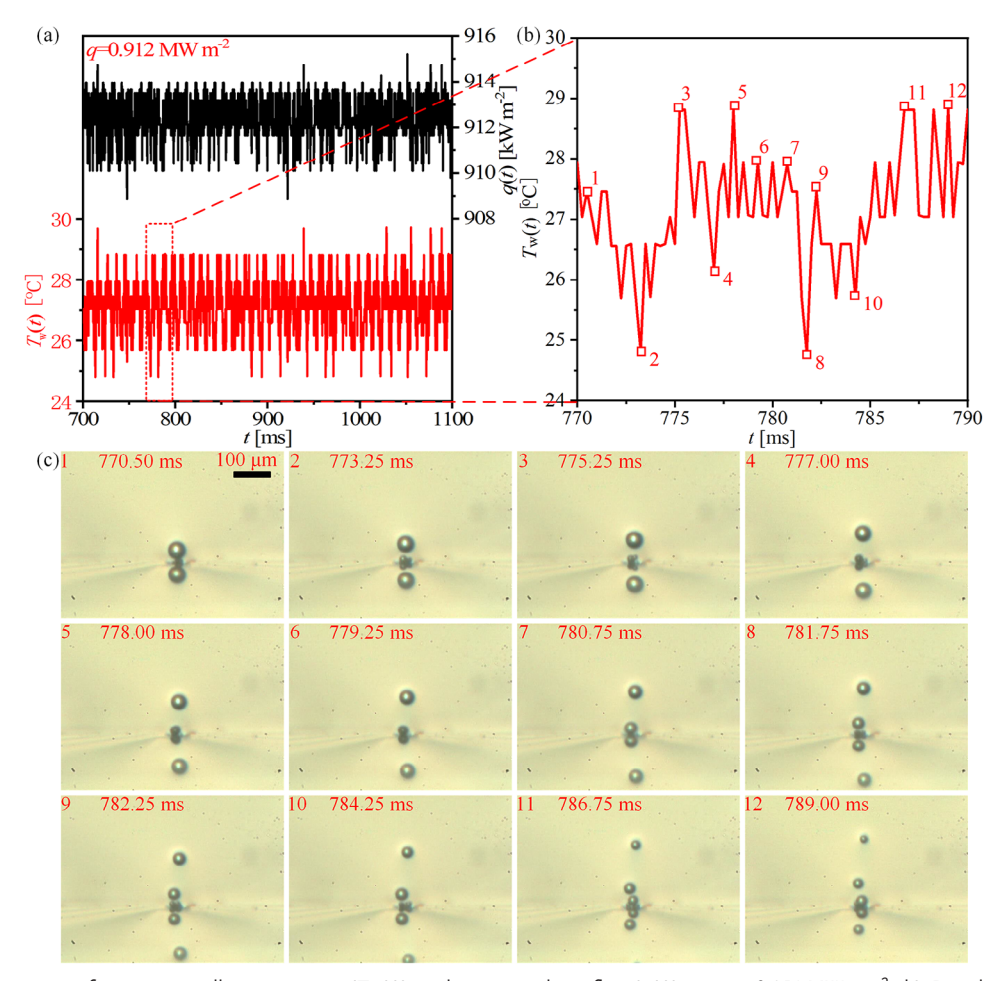


Figure 2. a) Fluctuations of transient wall temperature ($T_{\rm w}(t)$) and transient heat flux (q(t)) at $q=0.912\,{\rm MW~m^{-2}}$. b) Detailed wall temperature fluctuations at 770–790 ms. c) Corresponding visual images at 770.5–789 ms.

16136829, 0, Downloaded from https://onlinelibrary.wiley.com/doi/10.1002/smll.202411835 by North China Electric Power University Beijing, Wiley Online Library on [23/10/2025]

litions) on Wiley Online Library for rules of use; OA articles are governed by the applicable Creative Common

www.small-journal.com

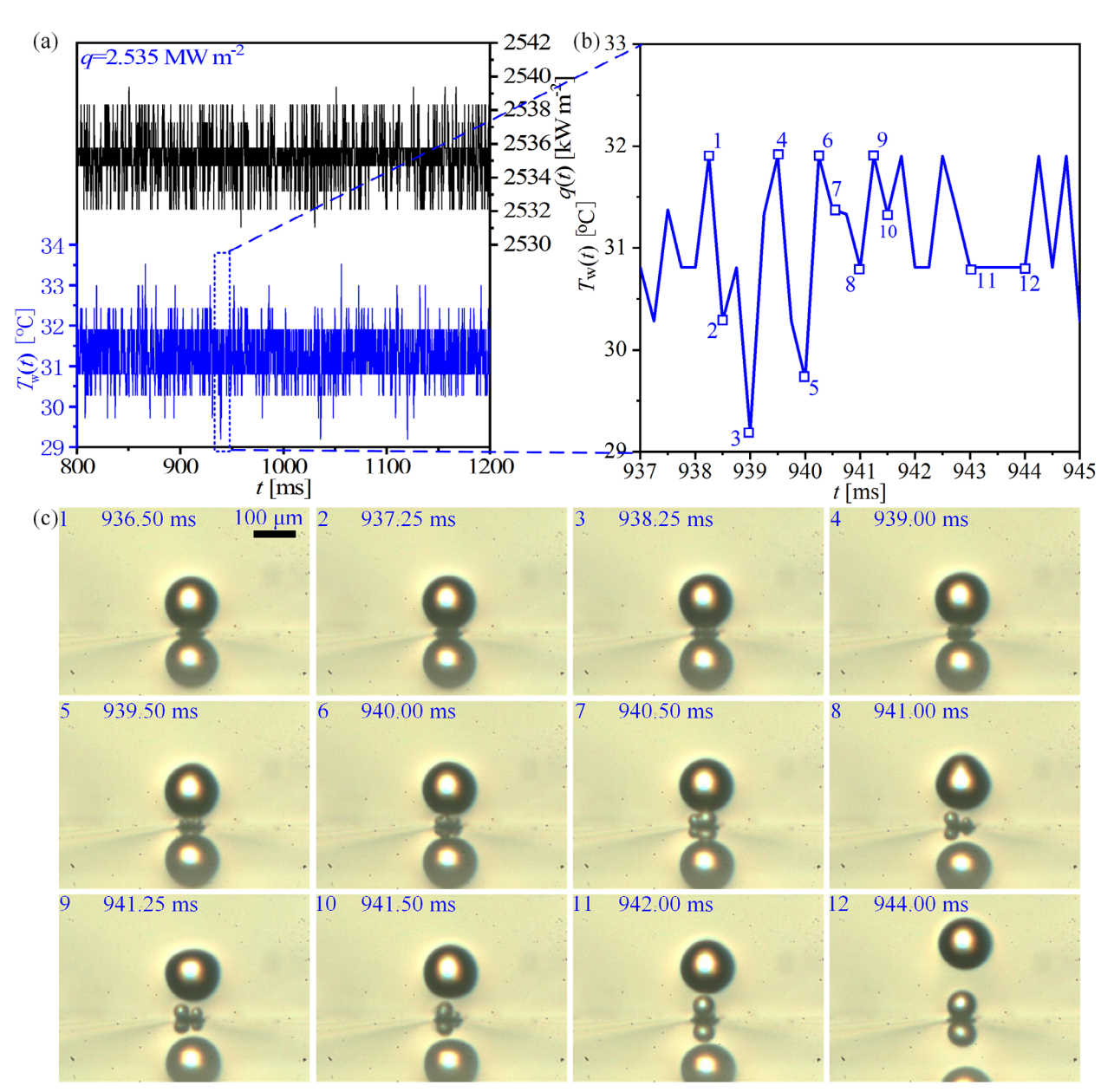


Figure 3. a) Fluctuations of transient wall temperature ($T_w(t)$) and transient heat flux (q(t)) at $q=2.535\,\mathrm{MW}\,\mathrm{m}^{-2}$. b) Detailed wall temperature fluctuations at 937–945 ms. c) Corresponding visual images at 936.5–944 ms.

large bubbles but also by the nucleation of micro bubbles and their subsequent merging. These interactions introduce significant irregularities in the $T_{\rm w}(t)$ fluctuations, suggesting that heat transfer in this region is modulated by the combined effects of both large and micro bubble nucleation.

In the high heat flux region of the Convective Boiling (CB) mode (q = 4.093-8.290 MW m⁻²), the fluctuations in $T_{\rm w}(t)$ and q(t) markedly diverge from those observed in the nucleate boiling (NB) region. The data here exhibit more pronounced oscillations with distinct peaks and troughs, as shown in **Figure 4a**. Visual inspections reveal a heightened level of activity involving both large and micro bubbles, leading to intricate $T_{\rm w}(t)$ fluctuations. The expanded plot of $T_{\rm w}(t)$ fluctuations in Figure 4b indicates that be-

tween 1340.5 ms and 1362.25 ms, $T_{\rm w}(t)$ experiences a significant decrease due to the sequential detachment of large bubbles (see Figure 4c). This cooling effect is ascribed to the convective motion induced by the movement of large bubbles, a phenomenon not encountered in the NB mode. In this high heat flux domain, heat transfer is predominantly driven by convection.

2.1.2. Bubble Diameter and Bubble Velocity

This part focuses on the dynamics of bubble formation during the boiling of carbon dioxide, scrutinizing parameters such as bubble diameter, frequency, and velocity (**Figure 5**). The figure

16136829, 0, Downloaded from https://onlinelibrary.wiley.com/doi/10.1002/smll.202411835 by North China Electric Power University Beijing, Wiley Online Library on [23/10/2025]. See the Terms and Conditions

conditions) on Wiley Online Library for rules of use; OA articles are governed by the applicable Creative Commons

www.small-journal.com

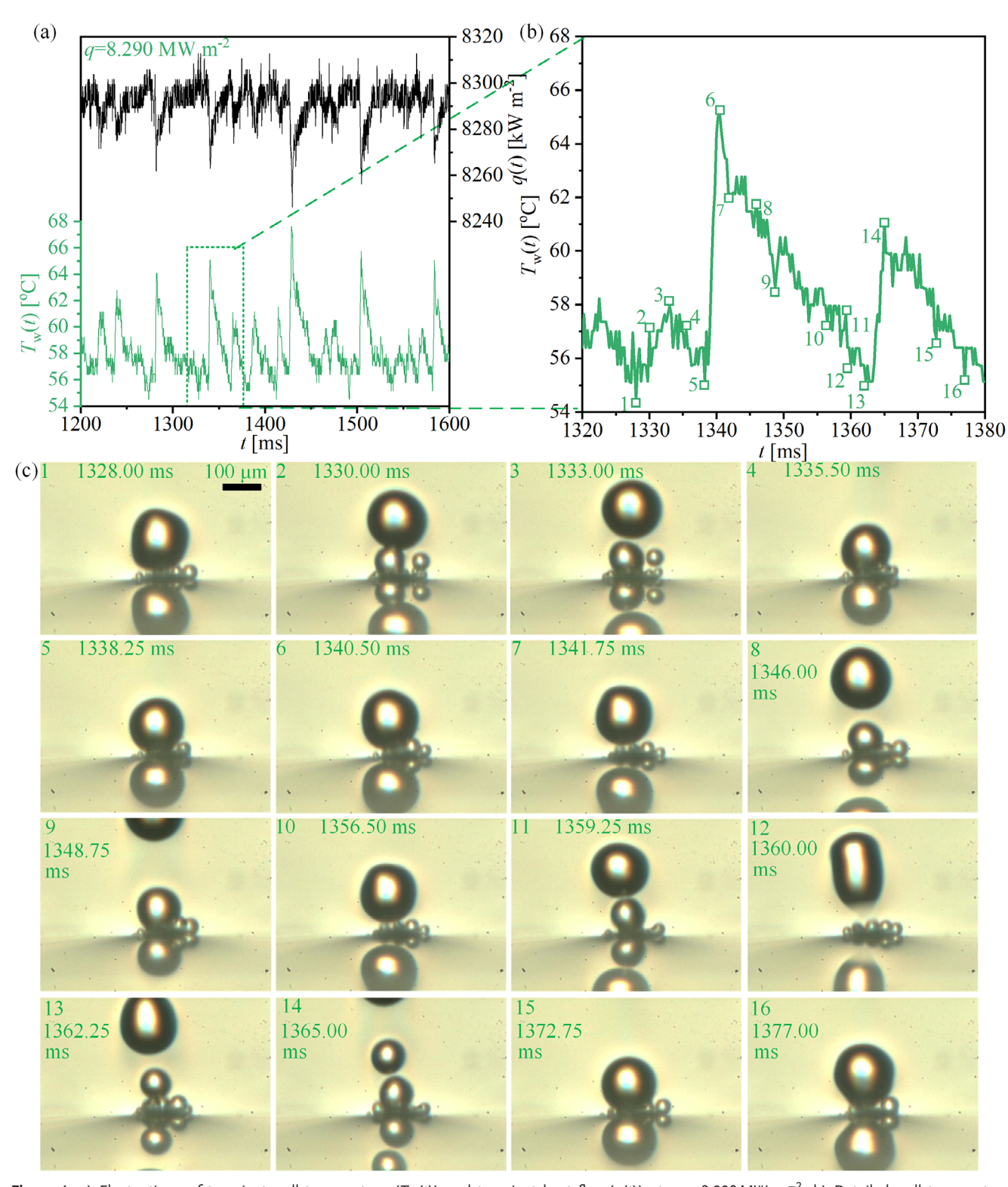


Figure 4. a) Fluctuations of transient wall temperature ($T_w(t)$) and transient heat flux (q(t)) at $q=8.290\,\mathrm{MW}$ m $^{-2}$. b) Detailed wall temperature fluctuations at 1340.5–1362.25 ms. c) Corresponding visual images at 1328–1377 ms.

www.small-journal.com

16136829, 0, Downloaded from https://onlinelibrary.wiley.com/doi/10.1002/sml1.202411835 by North China

Electric Power University Beijing, Wiley Online Library on [23/10/2025]. See the Terms

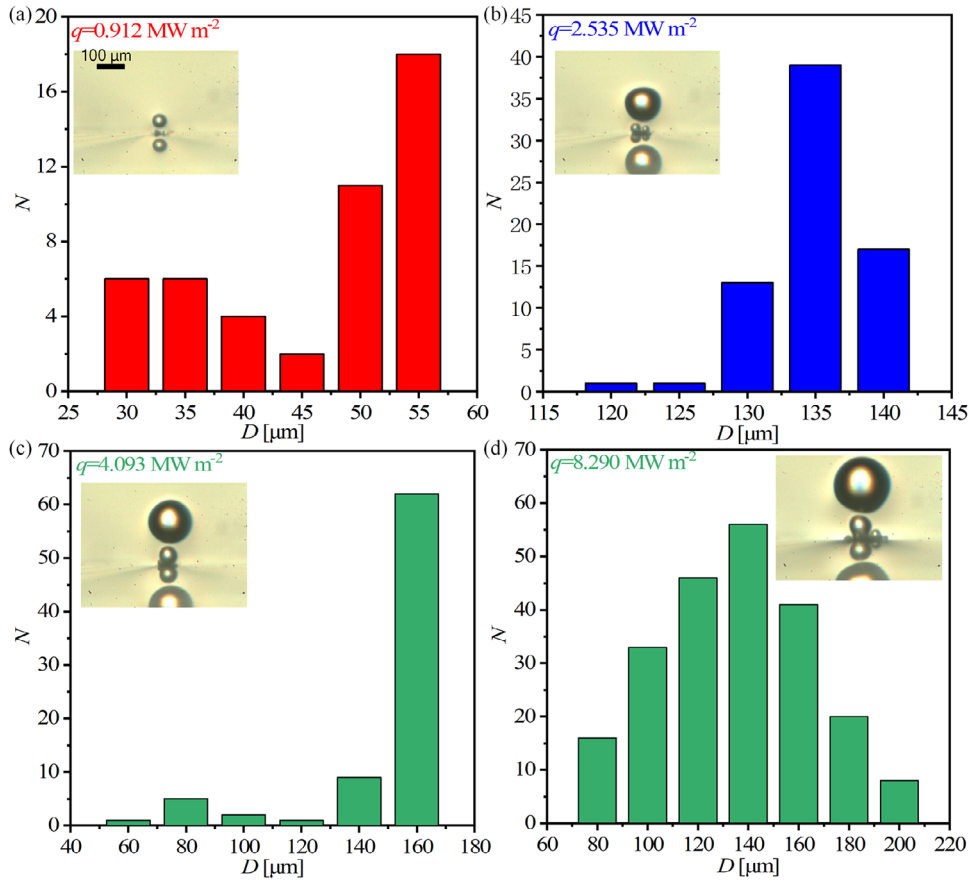


Figure 5. Statistical distribution of bubble departure diameter (D) at different heat fluxes. a) $q = 0.912 \text{ MW m}^{-2}$. b) $q = 2.535 \text{ MW m}^{-2}$. c) q = 4.093 MW m^{-2} . d) $q = 8.290 MW m^{-2}$.

also captures the visualization of the final moment of bubble detachment. The data reveal that at a heat flux of 0.912 MW m⁻², the majority of D values hover \approx 55 µm, whereas at 2.535 MW m^{-2} , these values escalate to $\approx 135 \mu m$. Notably, within the high heat flux region, D values tend to cluster at 160 µm for a heat flux of 4.093 MW m⁻², but exhibit greater heterogeneity at 8.290 MW m⁻², spanning from 100 to 180 μm. This heightened variability is ascribed to the intensified activity of micro bubbles in the high heat flux region, where both the quantity and dimensions of micro bubbles play a role in shaping the diameter of the ultimately detached bubbles.

The average bubble departure diameter (\overline{D}) was calculated and is depicted in Figure 6a. In the low and medium heat flux regions, \overline{D} increases almost linearly with the elevation of q. However, in

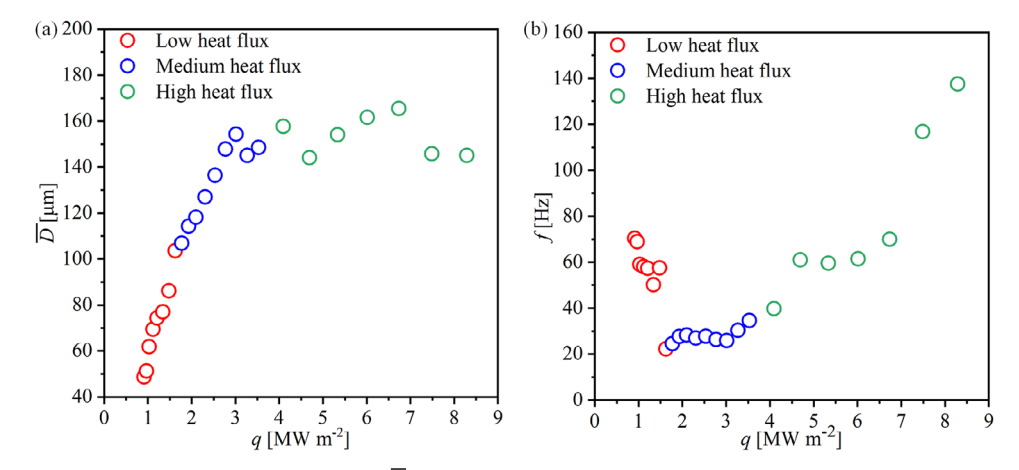


Figure 6. a) Variation of average bubble departure diameter (\overline{D}) with heat flux (q). b) Variation of average bubble frequency (f) with q.

16136829, 0, Downloaded from https://onlinelibrary.wiley.com/doi/10.1002/smll.202411835 by North China Electric Power University Beijing, Wiley Online Library on [23/10/2025]. See the Terms

xonditions) on Wiley Online Library for rules of use; OA articles are governed by the applicable Creative Common

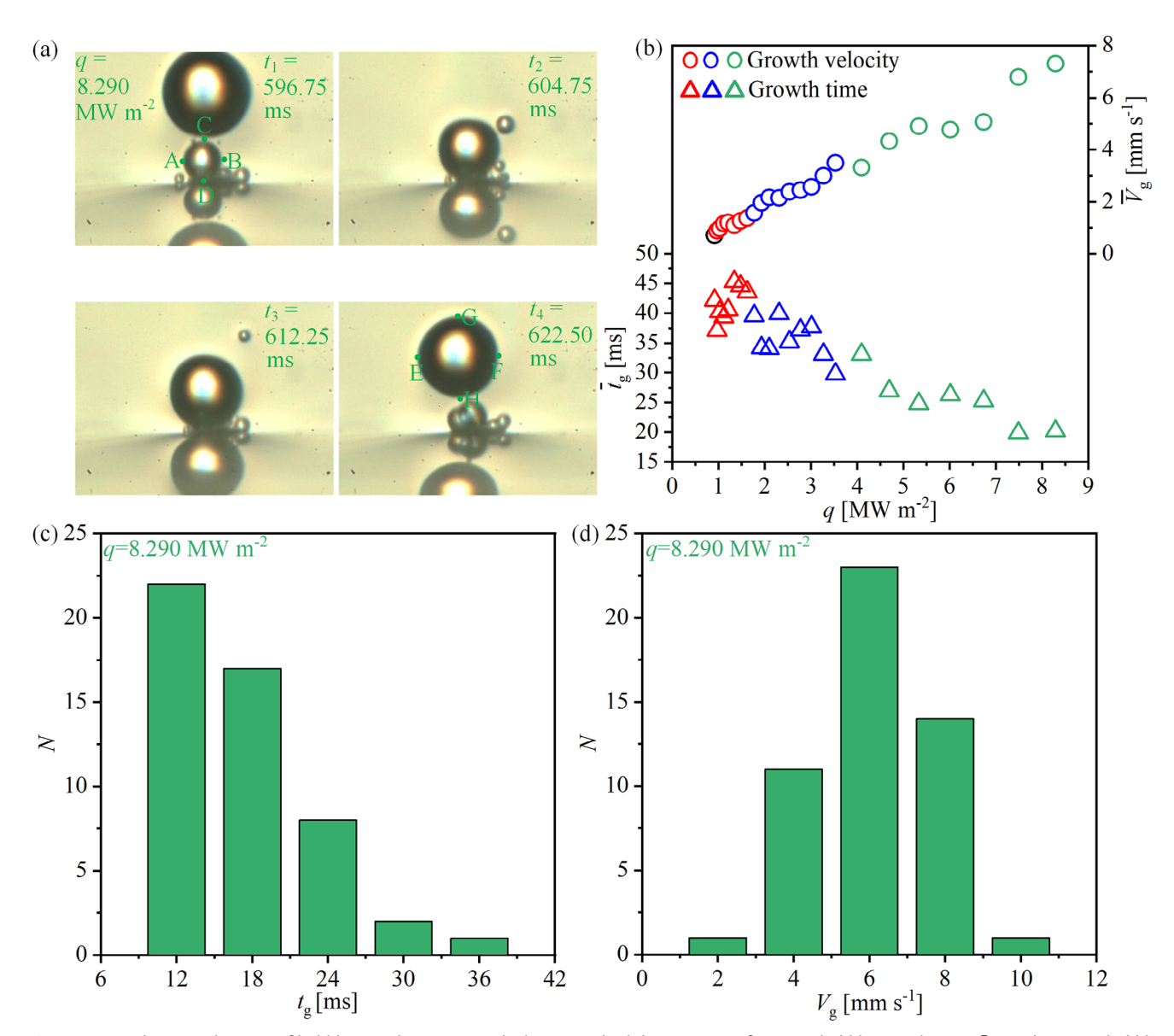


Figure 7. a) Schematic diagram of bubble growth time (t_g) calculation method. b) Variation of average bubble growth time $(\bar{t}g)$ and average bubble growth velocity $(\bar{V}g)$ with heat flux (q). c) Statistical distribution of t_g at q = 8.290 MW m⁻². d) Statistical distribution of V_g at q = 8.290 MW m⁻².

the high heat flux region, \overline{D} does not continue to rise consistently; instead, it plateaus within the range of 145–165 µm as q increases. Figure 6b shows the variation of the average bubble frequency (f) with q. In the low heat flux region, f decreases as q increases. This decline is attributed to the fact that as \overline{D} grows, the length of the three-phase contact line also augments, leading to increased surface tension that hinders bubble detachment. In the medium heat flux region, f increases gradually with q. This uptick occurs because the buoyancy force on the bubble increases at a faster rate than the growth of surface tension, thereby reducing the difficulty of detachment. In the high heat flux region, f ascends rapidly with q due to the presence of a multitude of micro bubbles at the base, which coalesce with large bubbles. These micro bubbles facilitate detachment, causing f to increase more precipitously.

The growth velocity ($V_{\rm g}$) and growth time ($t_{\rm g}$) of bubbles are examined, as illustrated in **Figure 7a**. The calculation of the bubble growth velocity is detailed as follows: The initial moment t_1 (596.75 ms) is identified when the bubble first forms into a complete sphere, with the leftmost and rightmost edges noted as points A and B, and the top and bottom edges as points C and D. The final moment t_4 (622.50 ms) is recorded when the bubble is fully detached and no longer interacts with micro bubbles at its base, with the leftmost and rightmost edges labeled as points E and F, and the top and bottom edges as G and H. To dissect the bubble growth dynamics, $t_{\rm g}$ and $V_{\rm g}$ are determined using Equations (1) and (2), respectively.

$$tg = t4 - t1 \tag{1}$$

16136829, 0, Downloaded from https://onlinelbtrary.wiley.com/doi/10.1002/smll.202411835 by North China Electric Power University Beijing, Wiley Online Library on [23/10/2025]. See the Terms

conditions) on Wiley Online Library for rules of use; OA articles are governed by the applicable Creative Commons

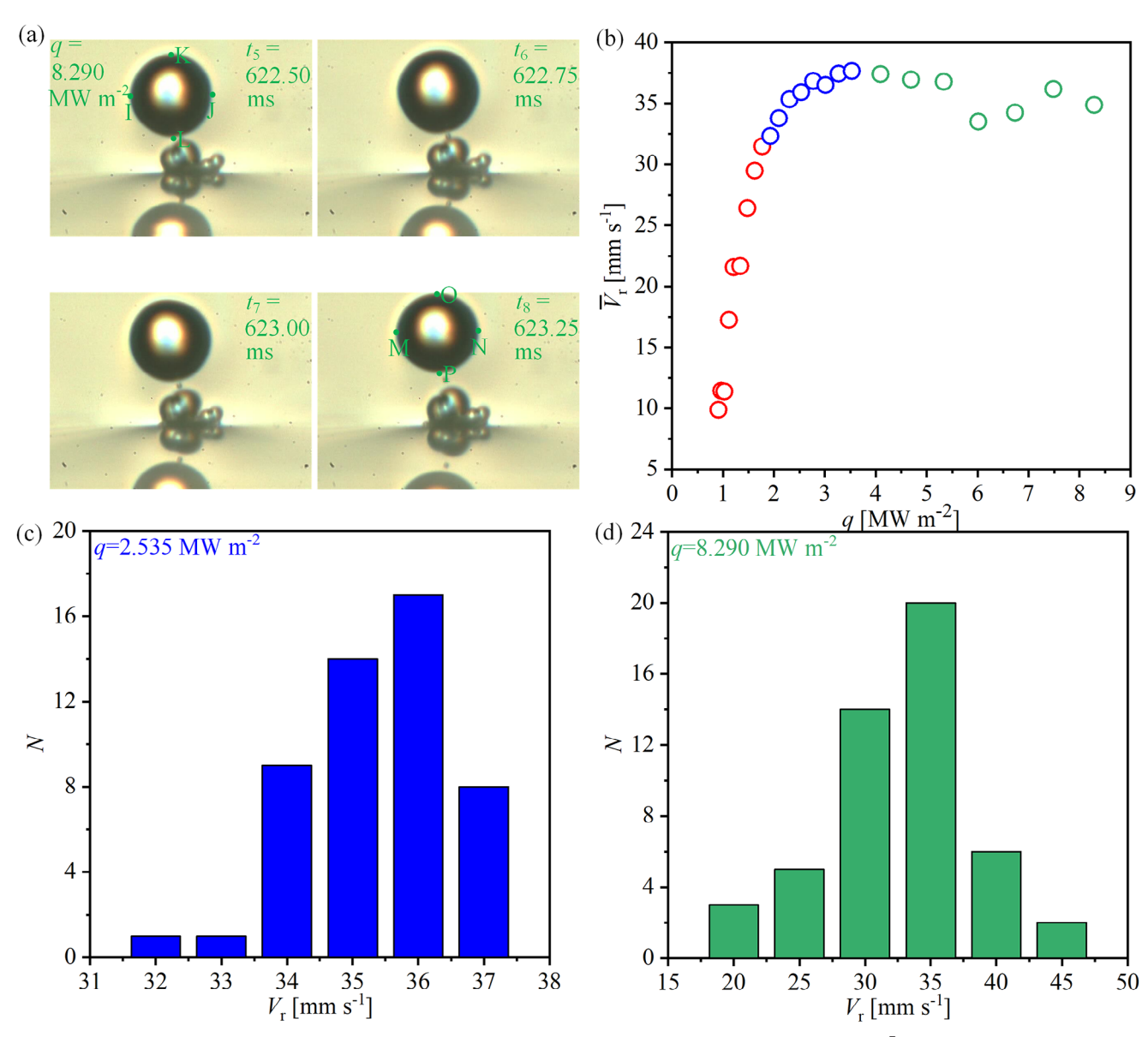


Figure 8. a) Schematic diagram of bubble rise velocity (V_r) calculation method. b) Variation of average rise velocity ($\bar{V}r$) with heat flux (q). c) Statistical distribution of V_r at q = 2.535 MW m⁻². d) Statistical distribution of V_r at q = 8.290 MW m⁻².

$$Vg = \frac{\sqrt{\left(\frac{XA + XB}{2} - \frac{XE + XF}{2}\right)^2 + \left(\frac{YC + YD}{2} - \frac{YG + YH}{2}\right)^2} \times 0.96525}{(t4 - t1) \times 10^6}$$
(2)

The experimental setup incorporated a high-speed camera with a frame rate of 4000 frames per second (fps) to ensure clear visualization of the bubble dynamics. The pixel length in the images captured was calibrated to 0.96525 μm , allowing for precise measurements of the bubble dimensions over time.

Fifty instances of bubble growth and detachment processes, analogous to those depicted in Figure 7a, were captured for each scenario, with the statistical outcomes displayed in Figure 7c,d. Specifically, for a heat flux of 8.290 MW m⁻² within the high heat flux region, t_g values are predominantly centered \approx 12 ms,

and $V_{\rm g}$ values are primarily focused at 6 mm s⁻¹. The average bubble growth time ($\bar{t}g$) and the average bubble growth velocity ($\bar{V}g$) were computed and are presented in Figure 7b. The findings indicate a trend where, as q escalates, $\bar{t}g$ diminishes while $\bar{V}g$ augments. This pattern suggests that the presence of micro bubbles significantly influences the acceleration of both the bubble growth and detachment processes in the high heat flux region.

The subsequent phase of the study focuses on determining the bubble rise velocity (V_r) post-detachment, as shown in **Figure 8a**. The methodology for calculating V_r is outlined below: The detachment of the bubble is marked by the initial moment t_5 (622.50 ms), which signifies the commencement of the bubble's ascent. The leftmost and rightmost edges at this instant are denoted as points I and J, respectively, with the top and bottom edges labeled as K and L. The final moment for the calculation of V_r is

xonditions) on Wiley Online Library for rules of use; OA articles are governed by the applicable Creative Common:

 t_8 (623.250 ms), with the corresponding edges labeled as M and N for the leftmost and rightmost, and O and P for the top and bottom. The V_r is then computed using Equation (3).

$$Vr = \frac{\sqrt{\left(\frac{XI+XJ}{2} - \frac{XM+XN}{2}\right)^2 + \left(\frac{YK+YL}{2} - \frac{YO+YP}{2}\right)^2} \times 0.96525}{(t8 - t5) \times 10^6}$$
(3)

For each scenario, 50 bubble rise processes akin to those in Figure 8a were captured, with the statistical outcomes presented in Figure 8c and Figure 8d. In the medium heat flux region, at q =2.535 MW m^{-2} , the V, values are predominantly concentrated between 35 and 36 mm s⁻¹. In contrast, in the high heat flux region, at $q = 8.29 \text{ MW m}^{-2}$, the V_r values exhibit a broader distribution, ranging from 30 to 35 mm s⁻¹. The average rise velocity (\bar{V} r) was determined by averaging the V_r values (see Figure 8b). The findings indicate that in the low and medium heat flux regions, Vr increases gradually with the increase of q. However, in the high heat flux region, $\bar{V}r$ does not continue to increase with q but instead stabilizes within the range of 33–34 mm s⁻¹. This observation suggests that once the large bubbles have completely detached from the micro bubble blanket, the facilitative effect of the micro bubbles vanishes, causing the large bubbles to lose their "power source". Consequently, the V_r values no longer escalate.

2.2. Micro Bubble Generation Analysis

In this research, liquid carbon dioxide serves as the heat transfer medium, leveraging its exceptionally low surface tension of 1.95 mN m⁻¹, which is approximately one-thirty-sixth that of water. This low surface tension significantly diminishes the nucleation energy barrier for bubble formation. Drawing from classical nucleation theory, the critical radius for homogeneous bubble nucleation (r_c) and the critical energy increment required for bubble formation ($\Delta \psi_c$) can be determined using Equations (4) and (5), respectively. [25] Additionally, the specialized micro-nano structure on the heating surface substantially amplifies the nucleation process by markedly increasing the density of active bubble nucleation sites. [26] At high heat fluxes, a continuous cycle of nucleation and merging of micro bubbles occurs on the heating surface concurrent with the growth and detachment of large bubbles. The low surface tension also aids in bubble coalescence, as it renders the liquid film between bubbles more prone to rupture. Vrij's research indicates the existence of a critical liquid film thickness (h_c) between bubbles (as Equation 6), which dictates whether the film ruptures and the bubbles coalesce. [27] When the actual liquid film thickness (h) is less than h_c , the film ruptures, permitting bubbles to merge. Micro bubbles can coalesce with each other, and before the detachment of a large bubble, these micro bubbles ultimately merge into it, a process termed as "departure" for micro bubbles. Following this merging, the punctured vapor neck left behind facilitates the swift reformation of new bubbles.[28]

$$rc = \frac{2\sigma T sat}{\rho vhlv (Tl - T sat)} \tag{4}$$

$$\Delta\psi c = \frac{4\pi\sigma rc^2}{3} \tag{5}$$

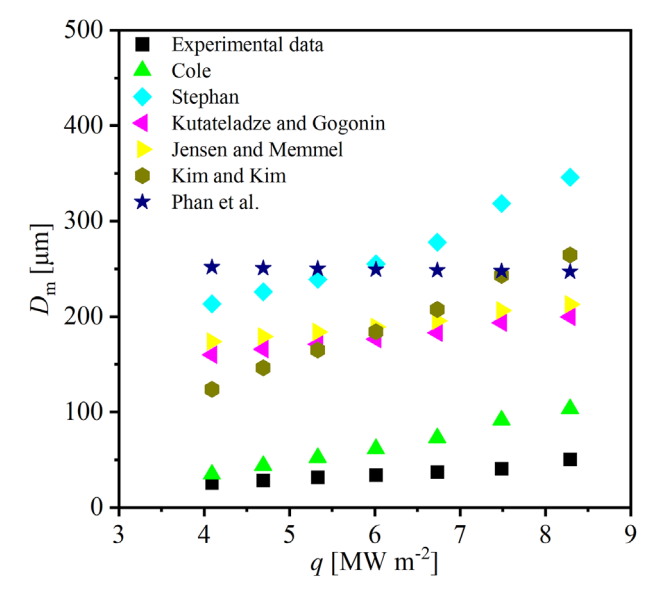


Figure 9. Comparison between experimental data and calculated results for micro bubble diameter (D_m) .

$$hc \sim 0.1(r^2AH/\sigma)^{1/4}$$
 (6)

where σ is the surface tension coefficient, T_{sat} is the saturation temperature, ρ_{v} is the density of vapor, T_{1} is the liquid temperature, h_{lv} is the latent heat of vaporization, r is the radius of the liquid film, and $A_{\rm H}$ is Hamaker constant.

Figure 9 shows the bubble departure diameters calculated using correlations for a smooth, flat surface (see Table 1). The comparison reveals that, in the majority of instances, the calculated departure diameters exceed the experimental measurements for individual micro bubbles. This discrepancy suggests that micro bubbles do not reach the conventional detachment diameters independently and are instead swept away by large bubbles.

The analysis of the diameter and number of micro bubbles (D_m and *n*) is presented below. It is noted that the existing relational correlations, which are heavily contingent on specific experimental conditions, yield predicted values that significantly deviate from the observed experimental data. This discrepancy suggests that these correlations are not readily applicable for calculating

Table 1. Correlations for bubble departure diameter.

Authors	Correlations
Kim and Kim ^[29]	$2Rd = 0.1649 Ja^{0.7} \sqrt{\frac{\sigma}{g(\rho l - \rho v)}}$
Cole ^[30]	$2R\mathbf{d} = 0.04 Ja \sqrt{\frac{2\sigma}{g(\rho \mathbf{l} - \rho \mathbf{v})}}$
Kutateladze and	$2Rd = 0.25[(1 + 10^5 K1) \frac{\sigma}{g(\rho l - \rho v)}]^{1/2} \text{for} K1 < 0.06$
Gogonin ^[31]	$K1 = \frac{Ja}{Pr1} \left\{ \left[\frac{g\rho I(\rho I - \rho v)}{\mu_I^2} \right] \left[\frac{\sigma}{g(\rho I - \rho v)} \right]^{3/2} \right\}^{-1}$
Jensen and Memmel ^[32]	$2Rd = 0.19(1.8 + 10^{5}K1)^{2/3} \sqrt{\frac{\sigma}{g(\rho l - \rho v)}}$
Stephan ^[33]	$2Rd = 0.25[1 + (\frac{Ja}{Pr})^2 \frac{100000}{Ar}]^{1/2} \sqrt{\frac{2\sigma}{g(\rho l - \rho v)}}$
	$Ar = (rac{ ho \lg(ho l - ho v)}{\mu_l^2})(\sqrt{rac{\sigma}{g(ho l - ho v)}})^3$, $\Pr = rac{\mu l Cpl}{\lambda l}$
Phan et al. ^[34]	$2Rd = 0.626977 \frac{(2+3\cos\theta-\cos^3\theta)}{4} \sqrt{\frac{\sigma}{g(\rho I - \rho v)}}, \text{ for } \theta \leq 90^\circ$

16136829, 0, Downloaded from https://onlinelibrary.wiley.com/doi/10.1002/smll.202411835 by North China Electric Power University Beijing, Wiley Online Library on [23/102025]. See the Terms and Conditions

conditions) on Wiley Online Library for rules of use; OA articles are governed by the applicable Creative Common

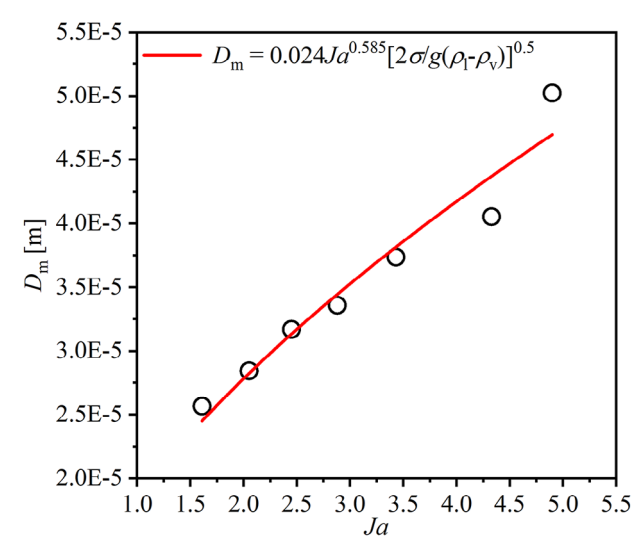


Figure 10. Fitting results for micro bubble diameter (D_m) .

the bubble detachment diameters in the context of this experiment. Nevertheless, the experimental findings demonstrate that the diameter of micro bubbles increases with both heat flux and superheat, aligning with the trend observed in existing correlations. Consequently, it is inferred that the diameter of micro bubbles is associated with surface superheat and the physical properties of the liquid, akin to the structure of existing correlations.

$$D\mathbf{m} = CJa^{m}\sqrt{2\sigma/g(\rho l - \rho v)} \tag{7}$$

$$Ja = \rho lc p l(Tw - Tsat) / \rho v h l v$$
(8)

where ρ_l is the density of the liquid, and c_{pl} is the constant pressure specific heat capacity.

To determine the values of C and m, the experimental data were fitted. From the images of the bubble just before detachment from the heating surface, the diameter of the micro bubble was measured. Based on the fitting results (Figure 10), the values obtained are C = 0.024 and m = 0.585. The correlation can thus be expressed as:

$$Dm = 0.024 J a^{0.585} \sqrt{2\sigma/g(\rho l - \rho v)}$$
(9)

Based on the law of conservation of energy and the law of conservation of mass, the number of micro bubbles can be calculated using the following formula:

$$n = \left(6V \cot - \pi D^3\right) / \pi D_m^3 \tag{10}$$

where V_{tot} is the total bubble volume, D is the diameter of the large bubbles, and $D_{\rm m}$ is the diameter of the micro bubbles. The detailed derivation process is provided in Note S1 (Supporting Information).

2.3. The Modified Bubble Dynamics Model

In this section, we explore the role of micro bubbles in facilitating the detachment of large bubbles during carbon dioxide pool boiling experiments. Through an analysis of the forces exerted during bubble growth, we have developed a modified model that elucidates the mechanism by which micro bubbles enhance the detachment of large bubbles. Utilizing this model, we predict the bubble departure diameter in high heat flux regions, finding that our predictions closely match the experimental data.

2.3.1. The Force Balance Analysis of Bubble

Generally the force impeding bubble detachment is termed the negative force, whereas the force promoting detachment is the positive force. As the liquid evaporates, bubbles expand; bubble detachment occurs when the positive force surpasses the negative force. In the medium heat flux region, as shown in Figure 11a, bubbles detach without micro bubble influence, permitting analysis via the traditional force balance model (see Figure S1, Supporting Information). This model identifies buoyancy $(F_{\rm b})$, differential pressure force $(F_{\rm p})$, and inertia force $(F_{\rm i})$ as positive forces, counterbalanced by drag force (F_d) and surface tension (F_s) as negative forces. In contrast, the high heat flux region, as illustrated in Figure 11b, is characterized by the continuous nucleation and merging of micro bubbles with large bubbles. Given the prevalence of micro bubbles, the interaction between large and small bubbles is considered as a form of surface tension, denoted as $F_{s tot}$. [35] Here, we employ a modified force balance model to dissect the forces acting on the bubble.

The expression of force balance is:

$$Fb + Fp + Fi = Fd + Fs, tot (11)$$

Surface tension at the vapor-liquid interface originates from the imbalance of molecular interactions along the liquid's surface, predominantly shaped by the properties of the liquid and the vapor interface. The traditional force balance model (Figure 11a) overlooks the interactions between bubbles. In this model, the surface tension for a bubble is presumed to be dependent on the radius of the contact line at the base of a large bubble (R_c) , formulated as $F_c = 2\pi\sigma R_c \sin\theta$. In the context of the modified force balance model, the force exerted at the base of a large bubble by an individual micro bubble is denoted as $F_{\rm m1}$, as depicted in the magnified view of Figure 11b. The direction of $F_{\rm m1}$ aligns with the tangent to the micro bubble, with its line of action at the contact line between the micro and large bubbles (denoted as R_{mc}). Consequently, this force is influenced by both the radius of the micro bubbles (R_m) and their quantity. Incorporating these elements yields the total surface tension:

$$Fs, tot = 2n\pi\sigma Rmc \sin\theta m \tag{12}$$

where $\theta_{\rm m}$ is the angle between the tangent direction of the micro bubble and the interface of the micro bubble and the large bubble, measured from the visual images as $\theta_{\rm m}$ = 43.5°. The relationship $R_{\rm mc} = R_{\rm m} {\rm sin} \theta_{\rm m}$ is then used to calculate $R_{\rm mc}$. The modified total surface tension is obtained using Equations (9), (10), and (12).

Beijing, Wiley Online Library on [23/10/2025]. See the Terms

ns) on Wiley Online Library for rules of use; OA articles are governed by the applicable Creative Co

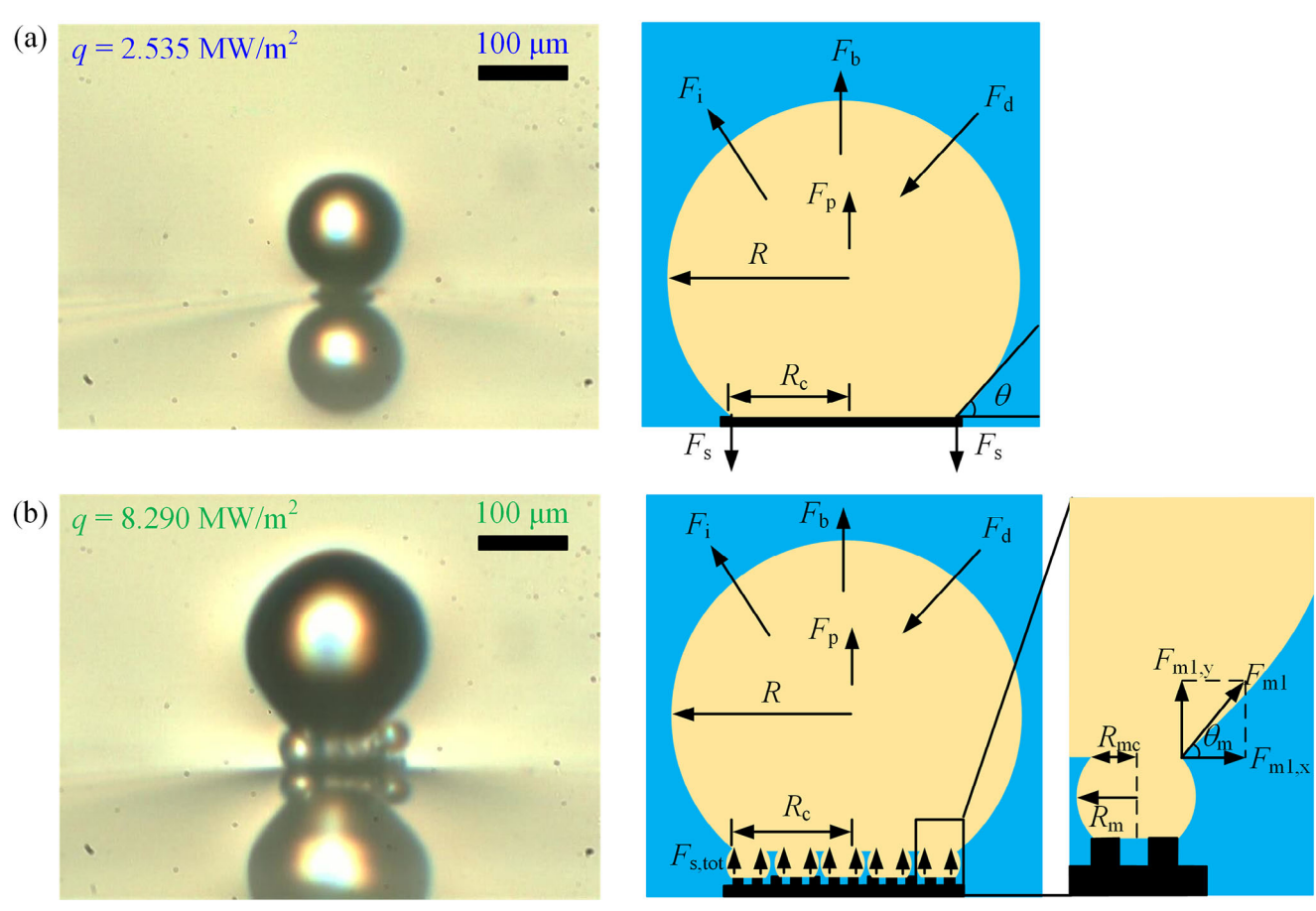


Figure 11. Visualizations and force analyses with and without the layer of micro bubble blanket. a) for medium heat flux region. b) for high heat flux region.

2.3.2. Comparison of the Prediction Results

The analysis presented establishes the correlation between the forces acting during bubble growth and the corresponding bubble diameters. **Figure 12a** illustrates the force-diameter relationship for the traditional force balance model under high heat flux region, with a heat flux of $q=8.290~{\rm MW~m^{-2}}$. Figure 12b offers a detailed view near the critical point where the bubble departure diameter is achieved, specifically when the net force ($F_{\rm net}$) is zero. Figure 12c depicts the force-diameter relationship using the modified force balance model under identical conditions ($q=8.290~{\rm MW~m^{-2}}$), and Figure 12d magnifies the view near the zero $F_{\rm net}$ point for the modified model. As shown in the figures, F_i , F_d , and F_b remain relatively constant and small throughout the bubble's growth, indicating that their influence on the bubble's growth is minimal. The pivotal forces that dictate the detachment of bubbles from the heating surface are $F_{\rm s,tot}$ and $F_{\rm p}$.

In the traditional force balance model, in the case of small bubbles, $F_{\rm s}$ exceeds $F_{\rm p}$, preventing bubble detachment and prompting continued growth on the heating surface. Detachment initiates when $F_{\rm net}$ equals zero, with the diameter at this point defined as the bubble departure diameter.

In the modified force balance model, when bubbles are in their nascent stage, numerous micro bubbles reside at their base, yet their diminutive sizes result in $F_{\rm s,tot}$ that exceeds $F_{\rm p}$. Consequently, the bubble persists in growing on the heating surface. Upon reaching a critical size, the micro bubbles at the base begin to coalesce horizontally, augmenting their diameter but reducing in number, which in turn diminishes $F_{\rm s,tot}$, while $F_{\rm p}$ escalates with the bubble's expansion. The transition of $F_{\rm net}$ from negative to positive signifies the bubble's detachment diameter, initiating its separation from the heating surface. Contrasting with the traditional model, where $F_{\rm s}$ and $F_{\rm net}$ trends are inverse, the modified model shows $F_{\rm s,tot}$ trending in concert with $F_{\rm net}$. This concordance underscores the pivotal role of inter-bubble interactions in the detachment of large bubbles. Furthermore, the force balance curve reveals that the traditional surface tension exceeds the modified total surface tension, implying that $F_{\rm s,tot}$ aids in the facilitation of bubble detachment.

In the traditional force balance model, surface tension and bubble diameter exhibit a negative linear relationship, whereas the modified force balance model reveals a positive relationship. Consequently, in the traditional model, bubble diameter must increase sufficiently for $F_{\rm p}$ to surpass $F_{\rm s}$ to enable detachment, particularly under high heat flux conditions. Figure 13a illustrates that at q=8.290 MW m $^{-2}$, the calculated bubble departure diameter is 234.54 µm, markedly larger than the experimental value of 145.08 µm. This divergence stems from the traditional

16136829, 0, Downloaded from https://onlinelibrary.wiley.com/doi/10.1002/sml1.202411835 by North China

Electric Power University Beijing, Wiley Online Library on [23/10/2025]. See the Terms

ms) on Wiley Online Library for rules of use; OA articles are governed by the applicable Creative Common

www.small-journal.com

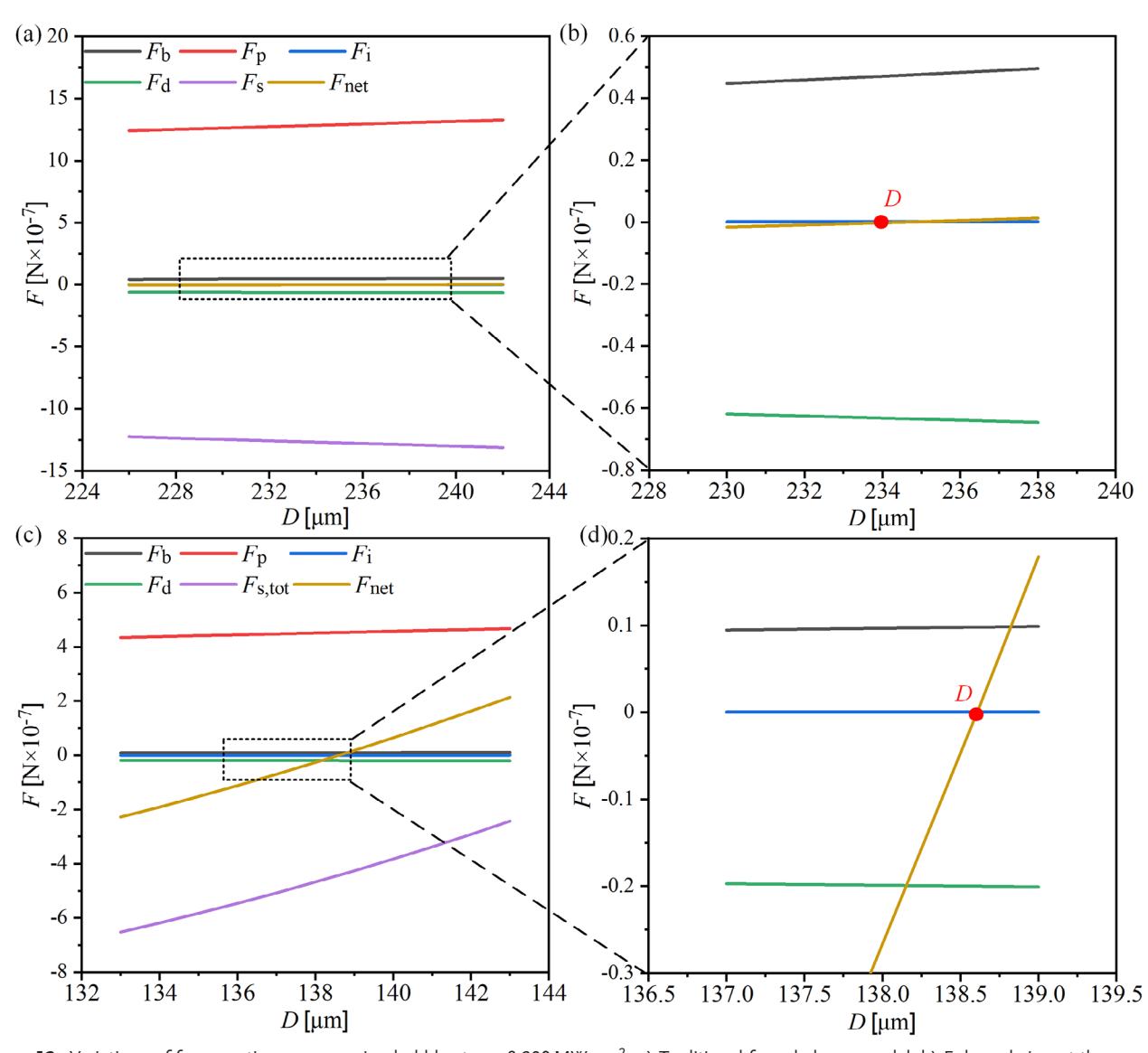


Figure 12. Variations of forces acting on a growing bubble at $q = 8.290 \,\mathrm{MW}\,\mathrm{m}^{-2}$. a) Traditional force balance model. b) Enlarged view at the zero net force point in the traditional force balance model. c) Modified force balance model. d) Enlarged view at the zero net force point in the modified force balance model.

model's omission of micro bubbles' role in facilitating large bubble detachment. Incorporating micro bubble effects in the modified force balance model prompts $F_{\rm net}$ to transition from negative to positive at a smaller diameter, enabling earlier detachment. Figure 13b shows that the calculated diameter of 138.61 μ m closely aligns with the experimental data of 145.08 μ m, with the bubble diameter trend matching experimental observations. As depicted in Figure 13, while the traditional model anticipates an increase in \overline{D} with rising q, the modified model mirrors the experimental data's trend of \overline{D} change with q.

3. Conclusion

In this study, we conducted micro-scale carbon dioxide pool boiling experiments utilizing a microheater with nanoscale thickness

under experimental pressures of 5.7 MPa and a pool temperature of 15 °C. High-speed imaging and simultaneous data collection elucidated the dynamics and heat transfer characteristics of micro-scale CO_2 boiling bubbles. Three distinct boiling heat transfer regimes were identified: Natural Convection (NC), Nucleate Boiling (NB), and Convective Boiling (CB). Heat transfer coefficients (h) in NC and NB modes increase with rising heat flux (q), while in CB, h exhibits a counterintuitive constancy despite increasing q.

Visual observations and synchronized data analyses revealed that in the low and medium heat flux regions of the Nucleate Boiling (NB) mode, the transient wall temperature $(T_w(t))$ and transient heat flow (q(t)) exhibited minimal fluctuations during bubble nucleation and departure. However, in the high heat flux region of the Convective Boiling (CB) mode, significant fluctuations in $T_w(t)$ and q(t) were observed, attributed to the

www.small-journal.com

16136829, 0, Downloaded from https://onlinelibrary.wiley.com/doi/10.1002/smll.202411835 by North China Electric Power University Beijing, Wiley Online Library on [23/10/2025]. See the Terms

on Wiley Online Library for rules of use; OA articles are governed by the applicable Creative Common

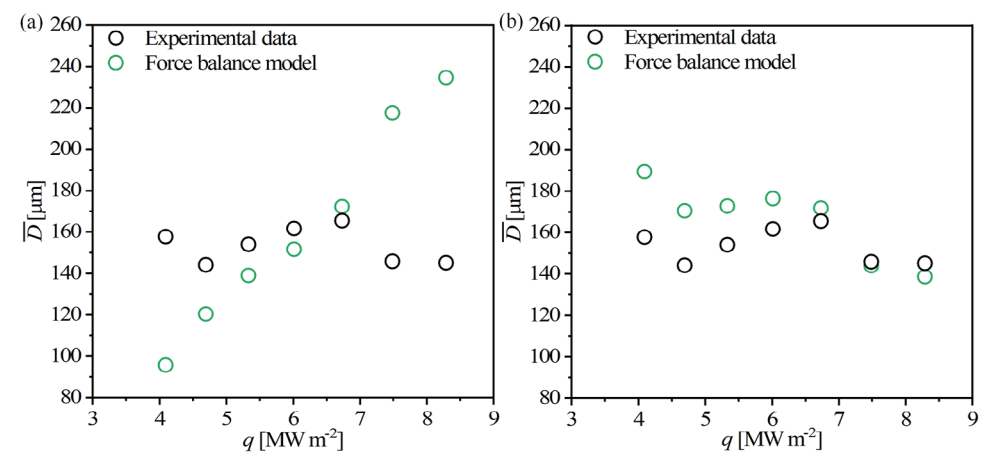


Figure 13. Comparison between calculated results and experimental data in the high heat flux region. a) Results obtained using the traditional force balance model. b) Results obtained using the modified force balance model.

successive departure of bubbles. Here, the bubble diameter and rise velocity at detachment were relatively stable, with the heat transfer process being predominantly influenced by the convective effects of bubble motion. To elucidate the rapid increase in bubble frequency (f) in the CB mode, we modified the traditional force balance model. The traditional force balance model neglects bubble interactions, whereas the modified force balance model incorporates the merging of micro and large bubbles and represents the interaction force as surface tension: $F_{s,tot}$ = $2n\pi\sigma R_{\rm mc}\sin\theta_{\rm m}$. While the traditional model displays a negative linear relationship between surface tension and bubble diameter, the modified model exhibits a positive linear relationship. This allows the net force (F_{net}) to reach zero at a smaller bubble diameter, facilitating earlier detachment. Quantitative calculations employing the modified model closely align with experimental data regarding bubble departure diameters in the high heat flux region.

4. Experimental Section

Microheater: In this study, microelectromechanical systems (MEMS) technology was utilized to fabricate a microheater with nanoscale thickness. The microheater was designed with platinum (Pt) as the heating resistor, gold (Au) as the electrode, and BF-33 (BOROFLOAT-33) glass as the substrate for metal sputtering. The physical configuration of the test section is depicted in Figure S2a (Supporting Information). Each microheater, measuring \approx 50 μ m \times 50 μ m, was arranged in a 3 \times 3 linear array, as shown in Figure S2b (Supporting Information). The microheater's composition, being platinum, allows its resistance to change linearly with temperature, thus functioning as a miniaturized resistance temperature detector (RTD) capable of both heating and temperature measurement. The 3D surface morphology, with the Pt layer highlighted in red (Figure S2c, Supporting Information), captured using a 3D profiler (Bruker Contour GT-K, Germany). The measured heights at $y = 20 \mu m$ and $y = 50 \mu m$, indicating a ridge height of ≈200 nm, are displayed in Figure S2d (Supporting Information). The heat transfer area was calculated to be $A = 4 \times (61 +$ = 1372 μm². The microheater was submerged in a constant-temperature water bath, with a current of ≈0.5 mA applied to the measurement circuit to ensure that the self-heating of the RTD was less than 0.1°C. Resistance measurements across various temperatures confirmed a linear relationship between resistance and temperature for the microheater, as shown in Figure S3 (Supporting Information).

Experimental Setup: For the investigation of heat transfer in liquid carbon dioxide using a microheater, an experimental system was established, including a high-pressure vessel, a pressure/temperature control system, a high-speed camera, and a high-speed data acquisition system, as shown in Figure S4a (Supporting Information). The horizontal pressure vessel, fabricated from 304 stainless steel, was equipped with sapphire glass windows on both sides for optical access. Carbon dioxide was both introduced and vented from the top of the vessel through a pressure control mechanism, which also manages system pressure and purges noncondensable gases. Within the vessel, spiral copper tubes regulate the circulation of temperature-controlled water to maintain a stable internal environment (see Figure S4b,c, Supporting Information). A thermocouple passes through the front of the pressure vessel, and the microheater was connected to an external circuit via wiring. The spiral copper tube, thermocouple, and wiring were sealed with appropriate fittings to preserve the integrity of the experimental setup.

Supporting Information

Supporting Information is available from the Wiley Online Library or from the author.

Acknowledgements

The authors acknowledge the support from the National Natural Science Foundation of China (52206197, 52130608) and Fundamental Research Funds for the Central Universities (2023MS014).

Conflict of Interest

The authors declare no conflict of interest.

Data Availability Statement

The data that support the findings of this study are available from the corresponding author upon reasonable request.

Keywords

micro bubble, nano ridge, pool boiling heat transfer, robust thermal management

www.small-journal.com

16136829, 0, Downloaded from https://onlinelibrary.wiley.com/doi/10.1002/smll.202411835 by North China Electric Power University Beijing, Wiley Online Library on [23/10/2025]. See the Terms

conditions) on Wiley Online Library for rules of use; OA articles are governed by the applicable Creative Common

Received: December 6, 2024 Revised: April 2, 2025 Published online:

- [1] S. S. Anandan, V. Ramalingam, Therm. Sci. 2008, 12, 5.
- [2] Z. Zhang, X. Wang, Y. Yan, e-Prime-Adv. Electr. Eng., Electron. Energy 2021, 1, 100009.
- [3] N. A. Pambudi, A. Sarifudin, R. A. Firdaus, D. K. Ulfa, I. M. Gandidi, R. Romadhon, Alexandria Eng. J. 2022, 61, 9509.
- [4] Y. Sun, Y. Wang, L. Zhu, B. Yin, H. Xiang, Q. Huang, Energy 2014, 65, 264
- [5] Y. Wang, L. Ren, Z. Yang, Z. Deng, W. Ding, IEEE Trans. Power Electron. 2021, 37, 3024.
- [6] B. B. Kanbur, C. Wu, S. Fan, F. Duan, Energy 2021, 217, 119373.
- [7] M. Ghazivini, M. Hafez, A. Ratanpara, M. Kim, J. Therm. Anal. Calorim. 2022, 147, 6035.
- [8] B. B. Mikic, W. M. Rohsenow, J. Heat Transfer. 1969, 91, 245.
- [9] W. M. Rohsenow, Trans. ASME 1952, 74, 969.
- [10] F. D. Moore, R. B. Mesler, AIChE J. 1961, 7, 620.
- [11] F. Demiray, J. Kim, Int. J. Heat Mass Transfer 2004, 47, 3257.
- [12] C. Gerardi, J. Buongiorno, L. W. Hu, T. McKrell, Int. J. Heat Mass Transfer 2010, 53, 4185.
- [13] T. Yabuki, O. Nakabeppu, Int. J. Heat Mass Transfer 2014, 76, 286.
- [14] S. Narayan, T. Singh, S. Singh, A. Srivastava, Int. J. Heat Mass Transfer 2019, 134, 85.
- [15] H. Ze, F. Wu, S. Chen, X. Gao, Adv. Mater. Interfaces 2020, 7, 2000482.
- [16] C. K. Yu, D. C. Lu, T. C. Cheng, J. Micromech. Microeng. 2006, 16, 2092.

- [17] M. Ha, S. Graham, Appl. Phys. Lett. 2017, 111, 091601.
- [18] J. Xu, W. Ye, X. Yu, B. Zhang, Nano Lett. 2023, 23, 10021.
- [19] H. J. Lee, S. Y. Lee, Int. J. Multiphase Flow 2001, 27, 2043.
- [20] G. Hetsroni, A. Mosyak, Z. Segal, G. Ziskind, Int. J. Heat Mass Transfer 2002, 45, 3275.
- [21] W. Qu, I. Mudawar, Int. J. Heat Mass Transfer 2003, 46, 2755.
- [22] X. Yu, J. Xu, G. Liu, X. Ji, Int. J. Heat Mass Transfer 2021, 164, 120460.
- [23] E. Bellos, C. Tzivanidis, Energy Convers. Manag. 2019, 1, 100002.
- [24] Z. Zhang, J. Qiang, S. Wang, M. Xu, M. Gan, Z. Rao, T. Tian, S. Ke, Y. Zhou, Y. Hu, C. W. Leung, C. L. Mak, L. Fei, Small 2021, 17, 2103301.
- [25] V. P. Carey, Liquid-vapor phase-change phenomena: an introduction to the thermophysics of vaporization and condensation processes in heat transfer equipment, CRC Press, Boca Raton, Florida, USA 2020.
- [26] C. Li, Z. Wang, P. I. Wang, Y. Peles, N. Koratkar, G. P. Peterson, Small 2008, 4, 1084.
- [27] A. Vrij, Discuss. Faraday Soc. 1966, 42, 23.
- [28] H. Park, S. F. Ahmadi, T. P. Foulkes, J. B. Boreyko, Adv. Funct. Mater. 2024, 34, 2312088.
- [29] J. Kim, M. H. Kim, Int. J. Multiphase Flow 2006, 32, 1269.
- [30] R. Cole, AIChE J. 1967, 13, 779.
- [31] S. S. Kutateladze, I. I. Gogonin, Teplofiz. Vys. Temp. 1979, 17, 792.
- [32] M. K. Jensen, G. J. Memmel, presented at IHTC, San Francisco 1986,
- [33] K. Stephan, Degree Thesis, University of Auckland, Auckland, New Zealand 1992
- [34] H. T. Phan, N. Caney, P. Marty, S. Colasson, J. Gavillet, Int. J. Heat Mass Transfer 2009, 52, 5459.
- [35] J. Zhou, Y. Zhang, J. Wei, Appl. Therm. Eng. 2018, 132, 450.